Role of topological charges in the nonlinear optical response from Weyl semimetals

Amar Bharti[1] and Gopal Dixit[1,2,*]

[1]*Department of Physics, Indian Institute of Technology Bombay, Powai, Mumbai 400076, India*
[2]*Center for Computational Sciences, University of Tsukuba, Tsukuba 305-8577, Japan*

The successful realization of the topological Weyl semimetals has revolutionized contemporary physics. In recent years, multi-Weyl semimetals, a class of topological Weyl semimetals, has attracted broad interest in condensed-matter physics. Multi-Weyl semimetals are emerging topological semimetals with nonlinear anisotropic energy dispersion, which is characterized by higher topological charges. In this study, we investigate how the topological charge affects the nonlinear optical response from multi-Weyl semimetals. It has been observed that the laser-driven electronic current is characteristic of the topological charge, and the laser polarization's direction influences the current's direction and amplitude. In addition, the anomalous current, perpendicular to the laser's polarization, carries a distinct signature of the topological charges and encodes the information about the parity and amplitude of the nontrivial Berry curvature. We show that the anomalous current associated with the anomalous Hall effect remains no longer proportional to the topological charge at higher laser intensity—a significant deviation from the linear response theory. High-harmonic spectroscopy is employed to capture the distinct and interesting features of the currents in multi-Weyl semimetals where the topological charge drastically impacts the harmonics' yield and energy cutoff.

I. INTRODUCTION

Recent years have witnessed a proliferation in studies of quantum materials, such as topological insulators, Dirac and Weyl semimetals, as these materials are not only crucial for fundamental research but also have immense applications in upcoming quantum technologies. Owing to the presence of the topologically protected Weyl points, Weyl semimetals (WSMs) have become a focal point among the quantum materials [1–3]. Isolated points in momentum space at which valance and conduction bands, with linear energy dispersions, touch are known as Weyl points. These points appear in pairs with opposite chirality and can be visualized as the source and sink of the Berry curvature. The low-energy collective excitations in WSMs are massless Weyl fermions, which make an elegant connection between high-energy and condensed-matter physics.

The three-dimensional Dirac semimetals possess both time-reversal and inversion protection, giving fourfold degenerate Dirac points. If one of these two symmetries is broken, then these Dirac points transform into Weyl points. The absence of the time-reversal or inversion symmetry in the WSMs gives rise to the Berry curvature. The topology of the Berry curvature in WSMs results in a series of exotic phenomenons, such as the chiral magnetic effect [3–5], the circular photogalvanic effect [6–9], and the anomalous Hall effect [10–12] to name but a few [13–15]. Interaction of light with WSMs has been a frontier approach to probe various exotic phenomena associated with the Berry curvature in WSMs [16–25]. The

WSMs also hold promise for future technologies based on the ultrafast photodetector, the chiral terahertz laser source, and quantum physics [26,27].

Earlier realizations of the WSMs have a unit topological charge, $n = 1$ [28–32]. The sign of the Berry-curvature monopole determines the sign of the topological charge of the WSMs. The magnitude of the topological charge is $n = \int_{BZ} \nabla_{\mathbf{k}} \cdot \Omega(\mathbf{k})\, d\mathbf{k}$, with $\Omega(\mathbf{k})$ being the Berry curvature. A class of WSMs, multi-Weyl semimetals (m-WSMs), with topological charges higher than 1 came into existence in recent years. The m-WSMs with topological charges 2 and 3 are, respectively, manifested by quadratic and cubic energy dispersions along particular directions, whereas they exhibit linear dispersion along other directions [33–36]. This contrasts with "conventional" WSMs with topological unit charges, which exhibit isotropic linear energy dispersion. Weyl points in m-WSMs can be formed by annihilating Weyl points of the same chirality in WSMs with lower topological charges [37]. The upper bound on the topological charge in m-WSMs is limited to 3 by certain crystalline symmetries [33,35,38]. A few possible potential candidates for the m-WSMs are $SiSr_2$ and $HgCr_2Se_4$ [33–35].

The m-WSMs manifest unique quantum response due to the higher topological charges and resultant anisotropic energy dispersions [39]. It has been shown that the chirality accumulation is possible without a magnetic field due to higher topological charges [40]. A distinct chiral anomaly-induced nonlinear Hall effect, associated with the different topological charges in m-WSMs, has been discussed [41]. Moreover, transport properties are significantly altered in comparison to the single-WSMs [42–47]. It has been found that the anomalous Hall current in the nonperturbative regime

---
*gdixit@phy.iitb.ac.in

saturates, and the anomalous Hall conductivity scales linearly with the topological charges [20,48]. By employing the effective field theory, the signature of a non-Abelian anomaly in m-WSMs has been investigated [49].

In this work, we investigate how the nonlinear optical responses in m-WSMs are sensitive to the topological charges for different laser intensities. In the following, we show that the current, parallel to the laser's polarization, and the anomalous current, perpendicular to the laser's polarization, exhibit distinct behavior as a function of the laser's intensity for different topological charges. In addition, we demonstrate that the current is anisotropic in nature, which strongly depends on the direction of the laser polarization. Moreover, the anomalous current is sensitive to the line connecting the Weyl points. The parallel current increases linearly below a critical laser's intensity. However, above a critical intensity, the parallel current shows a nonlinear increment for different topological charges, and it starts saturating after another critical intensity. On the other hand, the anomalous current displays linear behavior for relatively larger intensity. The Berry-curvature driven anomalous current approaches similar values for different topological charges at large intensity limits. We employ high-harmonic spectroscopy to probe the distinct behaviors of the normal and anomalous currents in m-WSMs. It has been found that the topological charge drastically alters the harmonics' yield and energy cutoff.

II. THEORETICAL FRAMEWORK

Interaction of a m-WSM with an ultrashort intense laser pulse is simulated by solving density-matrix-based semiconductor Bloch equations in the Houston basis [50] as

$$\frac{\partial \rho_{cv}^{\mathbf{k}}}{\partial t} = \left[-i\epsilon_{cv}^{\mathbf{k}_t} - \frac{1}{T_2} \right] \rho_{cv}^{\mathbf{k}} + i\mathbf{E}(t) \cdot \mathcal{D}_{cv}^{\mathbf{k}_t} \left[\rho_{vv}^{\mathbf{k}} - \rho_{cc}^{\mathbf{k}} \right], \quad (1a)$$

$$\frac{\partial \rho_{vv}^{\mathbf{k}}}{\partial t} = i\mathbf{E}(t) \cdot \mathcal{D}_{vc}^{\mathbf{k}_t} \rho_{cv}^{\mathbf{k}} + \text{c.c.} \quad (1b)$$

Here, $\epsilon_{cv}^{\mathbf{k}_t}$ and $\mathcal{D}_{cv}^{\mathbf{k}_t}$ are, respectively, energy band gap and dipole matrix elements between conduction and valence bands at $\mathbf{k}_t$. In the presence of an intense laser, the crystal momentum changes from $\mathbf{k}$ to $\mathbf{k}_t$ as $\mathbf{k}_t = \mathbf{k} + \mathbf{A}(t)$, where $\mathbf{A}(t)$ as the vector potential of the laser and is related to the laser's electric field $\mathbf{E}(t)$ as $\mathbf{A}(t) = -\int_{-\infty}^{t} \mathbf{E}(t')dt'$. A phenomenological term T_2 is introduced to account for the decoherence between the hole and the electron during the light-matter interaction process. Fourth-order Runge-Kutta method is used to solve Eq. (1) numerically for ρ at each time step. The completely filled valence band ($\rho_{vv} = 1$) and the empty conduction band ($\rho_{cc} = 0$) are used as initial conditions. The dipole matrix element and the energy are obtained from eigenstates and eigenenergies by the diagonalizing Hamiltonian given in Eqs. (2)–(4) as discussed in Ref. [51].

The total current is evaluated as $\mathbf{J}(\mathbf{k}, t) = \sum_{m,n \in \{c,v\}} \rho_{mn}^{\mathbf{k}} \mathbf{p}_{nm}^{\mathbf{k}_t}$, with $\mathbf{p}_{nm}^{\mathbf{k}_t}$ being the momentum matrix-element. The total current is decomposed into two components: intraband and non-intraband currents. The intraband current is solely originating due to group velocity and can be expressed as $\mathbf{J}_{\text{intra}}(\mathbf{k}, t) = \sum_n \nabla_{\mathbf{k}} \epsilon_n^{\mathbf{k}_t} \rho_{nn}^{\mathbf{k}}$. On the other hand, the non-intraband current contains the

contribution due to the Berry curvature, among others [52]. The Berry curvature is expressed in terms of the curl of the Berry connection: $\mathbf{\Omega} = \nabla \times \mathcal{A}$. The Berry connection between conduction and valence bands can be evaluated as $\mathcal{A}_{cv}(\mathbf{k}) = -i\langle \nabla_{\mathbf{k}} u_c(\mathbf{k}) | u_v(\mathbf{k}) \rangle = \mathcal{A}_{vc}^*(\mathbf{k})$, which is visualized as the off-diagonal dipole matrix elements [53,54]. Thus, the Berry curvature between conduction and valence bands is written as $\mathbf{\Omega}_{cv}(\mathbf{k}) = i[\mathcal{A}_{vc}(\mathbf{k}) \times \mathcal{A}_{cv}(\mathbf{k})]$. The current due to the Berry curvature is evaluated as $\mathbf{J}_{\mathbf{\Omega}}(\mathbf{k}, t) = \mathbf{E}(t) \times \sum_{cc,vv} \mathbf{\Omega}_{cv}(\mathbf{k}) \rho_{cc,vv}(\mathbf{k}, t)$ and is commonly known as the anomalous current.

Inversion-symmetric m-WSM with broken time-reversal symmetry for different topological charges n can be collectively written as $\mathcal{H}^{(n)}(\mathbf{k}) = \mathbf{d}^{(n)}(\mathbf{k}) \cdot \sigma$, with σ's being the Pauli matrices and $\mathbf{d} = [d_x, d_y, d_z]$ [49]. The full expressions of the three components of $\mathbf{d}^{(n)}(\mathbf{k})$ for topological charges $n = 1, 2$, and 3 are written as

$$\begin{aligned} \mathbf{d}^{(1)}(\mathbf{k}) = [&t\sin(k_x a), t\sin(k_y a), \\ &t\{\cos(k_z a) - \cos(k_0 a) + 2 - \cos(k_x a) - \cos(k_y a)\}], \end{aligned}$$
$$(2)$$

$$\begin{aligned} \mathbf{d}^{(2)}(\mathbf{k}) = [&t\{\cos(k_x a) - \cos(k_y a)\}, t\sin(k_x a)\sin(k_y a), \\ &t\{\cos(k_z a) - \cos(k_0 a) + 2 - \cos(k_x a) - \cos(k_y a)\}], \end{aligned}$$
$$(3)$$

and

$$\begin{aligned} \mathbf{d}^{(3)}(\mathbf{k}) = [&t\sin(k_x a)\{3\cos(k_y a) - \cos(k_x a) - 2\}, \\ &t\sin(k_y a)\{3\cos(k_x a) - \cos(k_y a) - 2\}, \\ &t\{\cos(k_z a) - \cos(k_0 a) + 2 - \cos(k_x a) - \cos(k_y a)\}]. \end{aligned}$$
$$(4)$$

Here, k_0 determines the positions of the Weyl nodes, which we have taken to be $k_0 = \pi/(2a)$ in this article throughout, unless stated otherwise. Thus, the positions of Weyl points for Eqs. (2)–(4) are $(0, 0, \pm k_0)$ as shown in Fig. 2.

III. RESULTS AND DISCUSSION

Let us apply a laser polarized along the z direction to induce electron dynamics in m-WSMs. Figure 1 presents the total current in m-WSMs with different topological charges. The current in a WSM with $n = 2$ is approximately 1 order higher in magnitude in comparison to the current for $n = 1$. However, the total current is comparable for $n = 2$ and 3 as evident from Fig. 1. The overall shape of the currents in all cases are significantly distorted with respect to the shape of the laser's electric field as shown in the inset. This distortion indicates the involvement of nonlinear optical processes during electron dynamics. Note that the laser polarized along the z direction does not yield current along any direction other than the polarization direction, which will be discussed later.

To understand the unusual behavior in the strength of the total current for different n values, let us first analyze the energy band structures of the m-WSMs. Owing to a similar structure of $\mathcal{H}^{(n)}(\mathbf{k})$, the eigenvalues can be succinctly written as $E_{c,v} = \pm\sqrt{d_x^2 + d_y^2 + d_z^2}$, where $E_{c,v}$ corresponds to
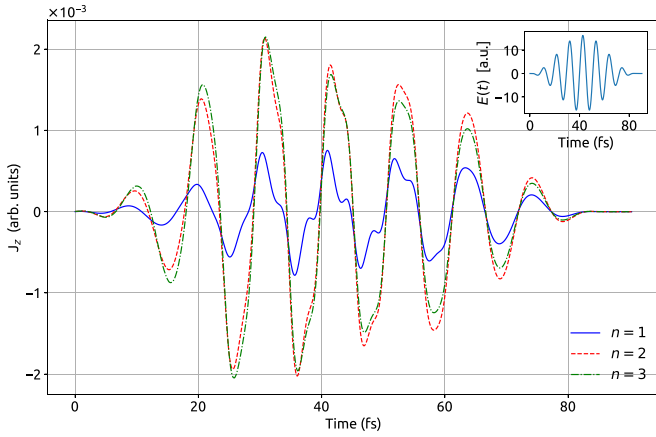
FIG. 1. Total current along the z direction in multi-Weyl semimetals for different topological charges n. The linearly polarized laser pulse along the z direction is employed to generate the current and is shown in the inset. The pulse is approximately 100 fs long with a wavelength of 3.2 µm and an intensity of 10^{11} W/cm^2. The value of the phenomenologically decoherence time T_2 is 1.5 fs.
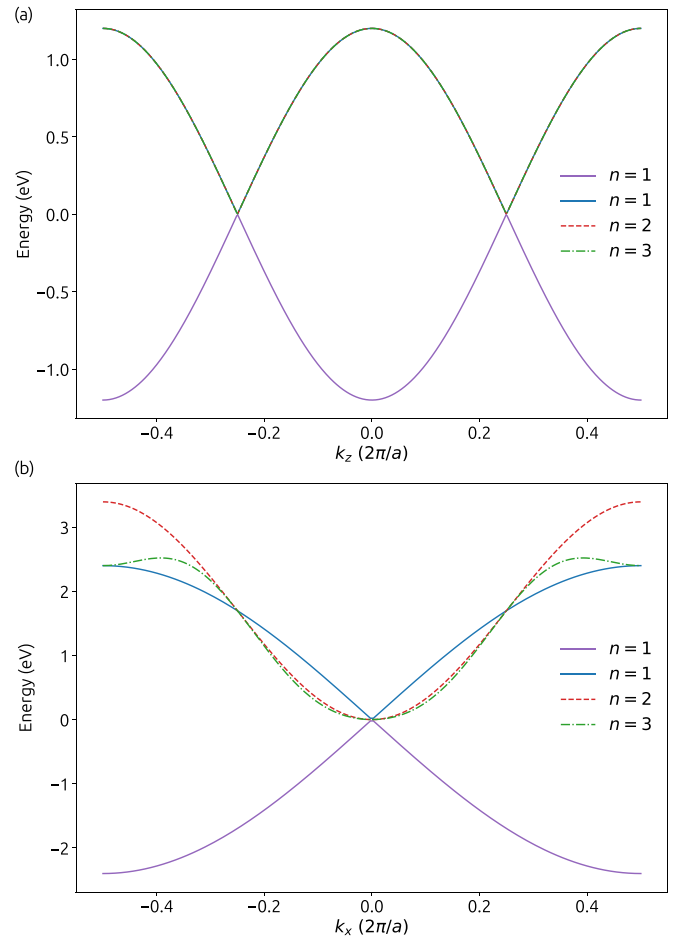

FIG. 2. Energy band structure corresponding to multi-Weyl semimetals with different topological charges along (a) the k_z direction and (b) the k_x direction around a Weyl node. The band structures along the k_y and k_x directions are identical. The band structure is obtained by diagonalizing the Hamiltonian $\mathcal{H}^{(n)}$ for different values of n with the hopping parameter $t = 1.2$ eV and the lattice parameter $a = 6.28$ Å. The purple line corresponds to the valence band in all cases.

conduction and valence bands, respectively; and the d's are corresponding **d**'s for each n as given in Eqs. (2)–(4).

Figure 2(a) shows the energy band structures along the k_z direction for different n values. The band structures with two Weyl nodes of opposite chirality at $\pm k_0$ are identical for $n = 1, 2,$ and 3 as evident from the figure. The reason behind the identical energy dispersion along k_z can be attributed to the same hopping parameter t and lattice parameter a for different n's. However, the band structures near one of the Weyl nodes are significantly different along k_x for different n's as documented in Fig. 2(b). Note that the band structures along k_x and k_y are identical. The different energy dispersions along k_x are directly related to the topological charges of the Weyl nodes. The relation between the energy dispersion and the topological charge is apparent from the low-energy Hamiltonian near a Weyl node as $\mathrm{H}^{(n)}(\mathbf{k}) = v(k_x^n \sigma_x + k_y^n \sigma_y + k_z \sigma_z)$ for $n = 1, 2,$ and 3. It is straightforward to see that the effective low-energy band structures are linear, quadratic, and cubic for $n = 1, 2,$ and 3, respectively. Furthermore, it can be shown explicitly by calculating Berry curvature that the Chern numbers corresponding to linear, quadratic, and cubic dispersions are 1, 2, and 3, respectively, as calculated elsewhere [44].

Analysis of Fig. 2 indicates that the current should be comparable for the m-WSMs with different n's as the energy dispersions are identical along the direction of laser polarization. However, the energy gap between valance and conduction bands is smaller for $n = 2$ and 3 in comparison to $n = 1$ around the Weyl node as evident from the energy dispersion along k_x, which translates into a higher probability of electron excitation for $n = 2$ and 3. Moreover, the energy dispersions for $n = 2$ and 3 are similar. The distinct energy dispersion naturally leads to the distinct gradient of the group velocity. Thus, the cubic band dispersion offers a larger intraband current compared to the quadratic one. Similarly, the linear dispersion has the smallest current flow out of the three. Both these facts explain why the total current exhibits similar features for $n = 2$ and 3 and is higher in magnitude

in comparison to $n = 1$. Note that the entire Brillouin zone contributes to the total current in three-dimensional systems like WSMs [55].

So far, we have witnessed that the laser polarized along the z direction does not generate current along any perpendicular direction. Let us see how this observation is modified when the polarization of the laser is tuned from the z direction to the x direction. Figure 3(a) presents the current parallel to the laser polarization for different topological charges. The strength of the current is drastically different for different n's, which is expected from the band structures along k_x as shown in Fig. 1(b). The current increases monotonically as the band dispersion goes from linear to quadratic and cubic with the increase in n. This observation is in contrast with the previous one where the current was comparable for $n = 2$ and 3. Before we delve into the detailed reason for the increase in current as a function of n, let us focus on the perpendicular component of the total current along the y direction as shown in Fig. 3(b). A similar perpendicular component appears along the x direction
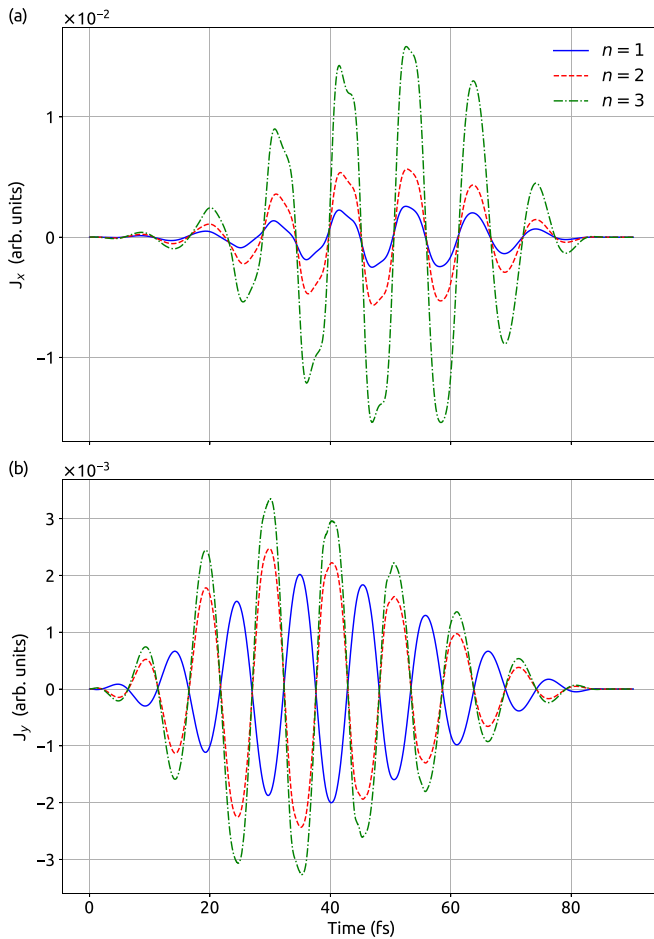
FIG. 3. Total current along (a) the direction of the laser polarization, i.e., normal current, and (b) along the perpendicular y direction, i.e., anomalous current. The laser is polarized along the x direction. Details of the simulation and the laser parameters are the same as those in Fig. 1.

when the laser is polarized along the y direction. In the following, let us use the terminology normal and anomalous currents for the currents along and perpendicular to the laser polarization, respectively, as used in a previous study [56].

We employ a semiclassical equation of motion for laser-driven electron dynamics to understand why the x-polarized laser generates anomalous current, whereas z polarization does not. It is known that the WSM has a nonzero Berry curvature, which results an anomalous velocity as $\mathbf{E}(t) \times \mathbf{\Omega}$. Moreover, the Berry curvature in an inversion-symmetric WSM follows $\mathbf{\Omega}(-\mathbf{k}) = \mathbf{\Omega}(\mathbf{k})$, which leads to nonzero current due to the anomalous velocity of $\int_{\mathbf{k}} \rho(\mathbf{k})\{\mathbf{E} \times \mathbf{\Omega}(\mathbf{k})\}d\mathbf{k}$. The parity of the Berry curvature's components in the present case (see Supplemental Material for details [57]) is such that there is no anomalous velocity if the electric field is along the same direction as the line connecting the Weyl nodes as discussed in Ref. [56]. Moreover, the anomalous current in the time-reversal broken WSM produces the anomalous Hall effect [58]. Thus, the anomalous current is zero when the laser is polarized along the z direction, the direction along which the two Weyl nodes are situated. The situation changes drastically as the polarization direction changes from z to x or y.

The anomalous current is proportional to $\mathbf{\Omega}$, which means it is also proportional to n. Thus, the strength of the anomalous current increases as n increases [see Fig. 3(b)]. However, the anomalous currents due to $n = 2$ and 3 are out of phase with respect to $n = 1$. This behavior is due to the sign of the integral of the Berry curvature's components as shown in Ref. [56]. The sign of $\int_{\mathbf{k}}\{\mathbf{E} \times \mathbf{\Omega}(\mathbf{k})\}d\mathbf{k}$ is positive for $n = 1$ and 3 and negative for $n = 2$, which leads the anomalous current for $n = 2$ out of phase. Thus, the strength and the phase of the anomalous current encode the information about the nontrivial topology of the Berry curvatures in m-WSMs. Note that the anomalous current is 1 order weaker than the normal current as evident from Fig. 3. At this juncture, it is interesting to wonder how these features in the normal and anomalous currents alter with the laser's intensity.

Figure 4 presents variation in the peak current for different n values as a function of the intensity ranging from 10^8 to 10^{11} W/cm^2. In the beginning, the anomalous current dominates over the normal current for each n at 10^8 W/cm^2. However, the normal current takes over the anomalous current at some critical intensity. On comparing the normal and anomalous currents for each n, we find that this critical intensity gets lower as n increases. In addition, the normal current starts to grow exponentially at a much lower intensity for higher n values. The peak current increases linearly as the intensity increases from 10^8 to 10^{10} W/cm^2 [see Fig. 4(a)]. Moreover, the rate of increase is much higher for the normal current as compared to the anomalous current, which starts to saturate at an intensity much lower than that of the normal current. There is no exponential growth region in the anomalous current compared to the normal current, which grows exponentially in the intensity window of 10^{10} to 10^{11} W/cm^2 [see Fig. 4(b)]. It is expected that the laser drives electrons further away in the energy band as the intensity increases, and therefore the normal current increases. However, the comparatively large anomalous current at lower intensity is interesting. Moreover, the subdued increment in the anomalous current needs further investigation. To understand these interesting observations, we analyze the laser-driven electronic population in the conduction band.

Electronic population in the conduction band for $n = 1$ is 1 order in magnitude weaker than the population for $n = 3$ as shown in Fig. 5(a). Moreover, the conduction band is sparsely populated for $n = 1$ at 10^8 W/cm^2. As the intensity increases from 10^8 to 10^{11} W/cm^2, the overall population increases by 2 orders in magnitude [see Fig. 5]. The conduction band population for $n = 3$ remains substantially more significant than that of the lower topological charges even at 10^{11} W/cm^2 as evident from Fig. 5(b). Similarly, the overall nature of the populations remains the same and the difference in populations is also pronounced for different n values at 10^9 W/cm^2 (not shown here). There are two key factors governing the overall behavior of the conduction band population for different n values at two intensities: the first one is the reduction in the energy gap between valence and conduction bands around a Weyl node as n increases [see Fig. 2(b)]. This results in higher probability of excitation and thus more population as n increases. The other important factor is the dipole matrix amplitude and its relation with n [see Eq. (1)], which manifests higher electronic population as n increases.
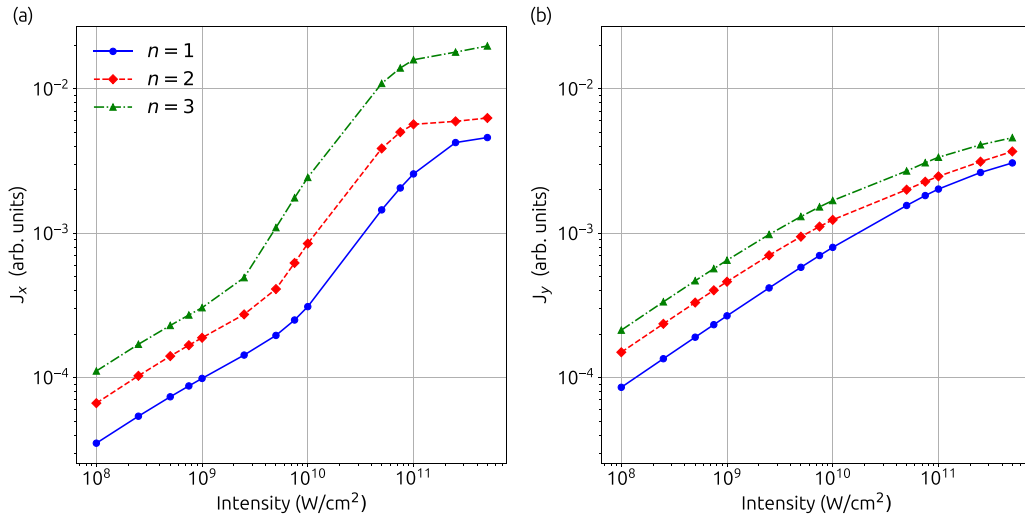
FIG. 4. Variations of the maximum amplitude for (a) the normal current along x and (b) the anomalous current along y as a function of the laser's intensity for multi-Weyl semimetals with topological charges $n = 1$, 2, and 3. The other parameters are the same as those in Fig. 3.

Thus, it can be concluded from Fig. 5 that the population increases monotonically with n irrespective of the laser's intensity.
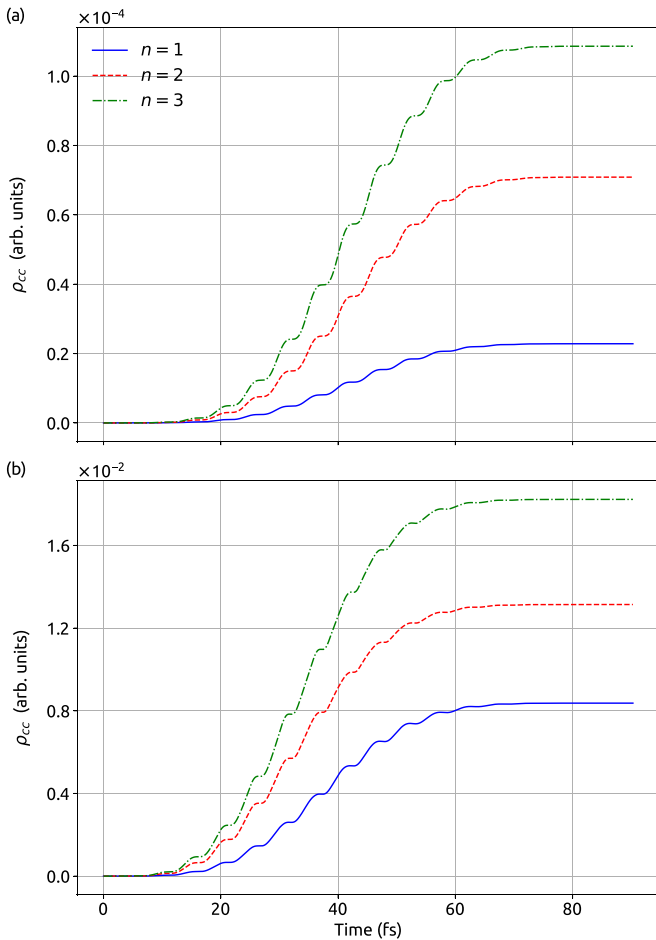

FIG. 5. Temporal evolution of the conduction band population ρ_{cc} for different n values during the laser for two intensities: (a) 10^8 W/cm^2 and (b) 10^{11} W/cm^2. The other parameters are the same as those in Fig. 3.

Returning back to the considerable anomalous current at the lowest intensity 10^8 W/cm^2, let us explore how the topological charge impacts the anomalous current. By following the analysis of the linear response from the WSM, the anomalous current is proportional to n as $\mathbf{J_\Omega} \propto n(\mathbf{b} \times \mathbf{E})$, where $\mathbf{b}$ is the vector joining the Weyl nodes [48]. The quantity $\mathbf{b} \times \mathbf{E}$ determines the direction of the anomalous current. Note that the same reasoning we have used earlier to explain why the laser polarized along the direction of the line connecting the Weyl nodes results in no anomalous current. If we consider the expression of $\mathbf{J_\Omega}$ to be true for the considered laser intensities then, the anomalous current should increase monotonically with intensity as $\mathbf{J_\Omega} \propto \mathbf{E}$. However, the anomalous current deviates significantly from this expectation at higher intensity, signaling a nonlinear optical response from m-WSMs. It is important to emphasis that the anomalous current along the perpendicular direction is mainly driven by the Berry curvature as shown in Fig. S1 [57].

To corroborate our claim about the nonlinear optical response, let us analyze the ratio of the anomalous current's peak for different n values as a function of the laser's intensity. The ratios of the peak current for $n = 3$ to $n = 1$ and $n = 2$ to $n = 1$ are presented in Fig. 6(a). Within the linear response framework, it is expected that the ratios $\mathbf{J_\Omega}|_{n=3}/\mathbf{J_\Omega}|_{n=1}$ and $\mathbf{J_\Omega}|_{n=2}/\mathbf{J_\Omega}|_{n=1}$ should be 3 and 2, respectively as $\mathbf{J_\Omega} \propto n$. This expectation is true at 10^8 W/cm^2 where the ratios are close to 3 and 2 as evident from Fig. 6(a). However, both ratios decrease monotonically as intensity increases, albeit at different rates. The ratios $\mathbf{J_\Omega}|_{n=3}/\mathbf{J_\Omega}|_{n=1}$ and $\mathbf{J_\Omega}|_{n=2}/\mathbf{J_\Omega}|_{n=1}$ reach approximately 2 and 1.5 at 10^{10} W/cm^2, respectively— a drastic deviation from the expectation of linear response theory. The ratio $\mathbf{J_\Omega}|_{n=3}/\mathbf{J_\Omega}|_{n=1}$ decreases with a much faster rate compared to $\mathbf{J_\Omega}|_{n=2}/\mathbf{J_\Omega}|_{n=1}$. This implies that the anomalous current due to the Berry curvature decreases faster with an increase in n. Thus, $\mathbf{J_\Omega}$ originating from two different topological charges may be comparable at a certain intensity. However, it is practically not feasible to keep increasing the intensity as it can go above the damage threshold of the material.
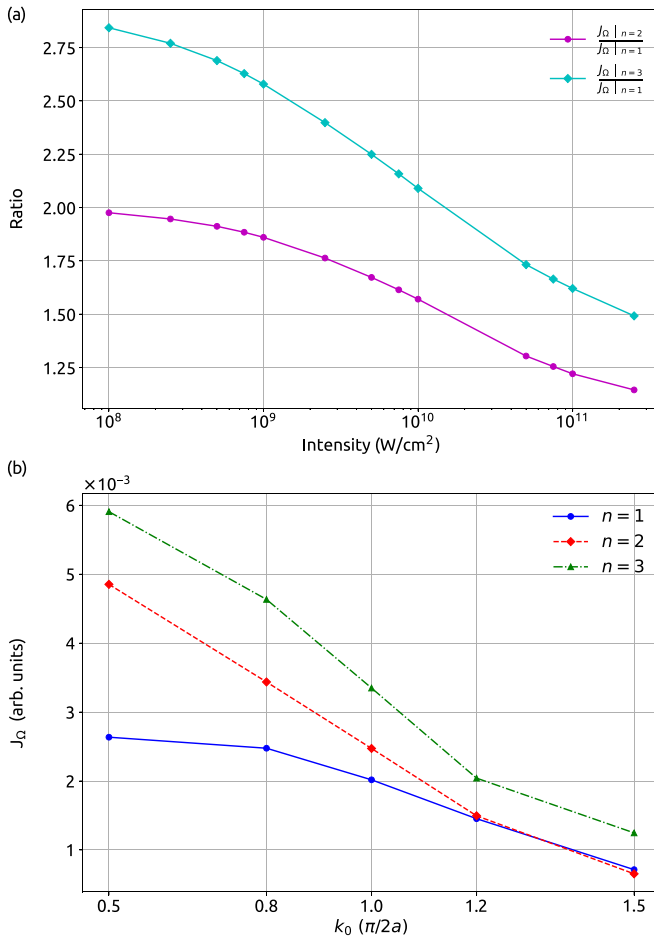
FIG. 6. (a) Ratio of the anomalous current's peak, $\mathbf{J_\Omega}$, as a function of the laser's intensity, and (b) variation in the anomalous current's peak, $\mathbf{J_\Omega}$, as a function of the separation between two Weyl nodes, k_0, at intensity 10^{11} W/cm^2 for different topological charges n.

FIG. 7. Higher-order harmonic spectrum corresponding to multi-Weyl semimetals with topological charges (a) $n = 1$, (b) $n = 2$, and (c) $n = 3$. The driving laser is 100 fs long with a wavelength of 3.2 μm and an intensity of 1×10^{11} W/cm^2. The laser pulse is linearly polarized along the x direction. A phenomenologically decoherence time T_2 of 1.5 fs is added in the simulation. The harmonic spectrum is simulated by taking the modules square of the Fourier transform of the time derivative of the total current as $|\mathcal{FT}(\frac{d}{dt}[\int \mathbf{J}(\mathbf{k}, t) \, d\mathbf{k}])|^2$ [60]. The distance between two Weyl node is $k_0 = \pi/(2a)$, with $a = 6.28$ Å.

So far, we have investigated how the anomalous current behaves with respect to the intensity. Recently, it has been shown that the nonlinear anomalous current in a Weyl semimetal with $n = 1$ decreases with increasing the distance between the Weyl nodes [56,59]. Let us see how the reported observation changes for m-WSMs. Figure 6(b) presents how the anomalous current's peak varies with the distance between the Weyl nodes for different n values. The current due to the Berry curvature decreases with an increment in the distance between the nodes, and the decrease is different for each n. Similar observations can be made when the intensity lies within the linear-response regime as evident from Fig. S2 [57]. The overall behavior of the anomalous current remains same, but the response due to the change in the distance is nontrivial when we compare for different n values.

The normal and anomalous currents are analyzed as the optical responses in m-WSMs, which transit from a linear regime to a nonlinear regime as the laser's intensity increases, even from a perturbative regime to a nonperturbative regime. High-harmonic generation (HHG) is a hallmark example of a nonperturbative nonlinear optical process, which has become a method of choice to probe various static and
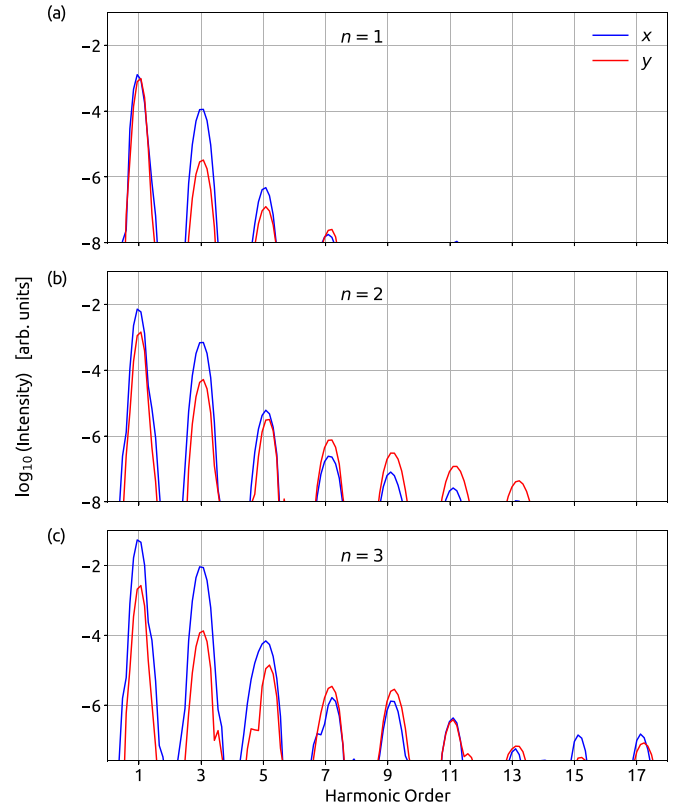
dynamical aspects of solids [50,61–69]. In addition, HHG from topological materials has become a center of attention as it allows one to investigate nonequilibrium topological aspects of topological insulators, Dirac and Weyl semimetals, in recent years [17,20,70–73]. Recently, it has been shown that high-harmonic spectroscopy can be used to probe the light-induced nonlinear anomalous Hall effect in a Weyl semimetal [56]. Thus, it is interesting to explore how the topological charge impacts HHG from m-WSMs.

The higher-order harmonic spectra corresponding to m-WSMs are distinct for different n's as can be seen from Fig. 7. Odd-order harmonics are only generated as m-WSMs exhibit inversion symmetry in the present case. The harmonic cutoff not only increases drastically but also the yield of the harmonics is boosted by several orders as n increases. The energy cutoff increases from 7 to 13 as n changes from $n = 1$ to $n = 2$. Moreover, the yield of the seventh harmonic is 2 orders in magnitude boosted as n transits from 1 to 2 as is evident from Figs. 7(a) and 7(b). Similar observations can be made for the harmonics shown in Fig. 7(c) for $n = 3$. The Berry-curvature-driven anomalous current in m-WSMs

results in anomalous odd harmonics along the y direction. The presence of the anomalous harmonics is a signature of the light-induced anomalous Hall effect, and the strength of these harmonics gives the measure of the Hall effect [56].

The characteristic dependence of the relative yield of the normal and anomalous harmonics on the harmonic order offers a route to tailor the polarization of the emitted harmonics, which carry information about the topology of the Berry curvature in m-WSMs. The ellipticity of the first, third, and fifth harmonics for $n = 1$ reads as 0.85, 0.17, and 0.55, respectively. As the value of the topological charge changes to $n = 2(3)$, the ellipticity of the first, third, and fifth harmonics changes drastically as 0.41(0.2), 0.25(0.11), and 0.72(0.45), respectively. The reduction of the ellipticity of a given harmonic with an increase in the topological charge can be attributed to a significant change in the yield of the anomalous harmonic. Thus, the ellipticity of the emitted harmonic for a given harmonic order is significantly different for different n values and can be potentially used as a characterization tool for the topological charge in m-WSMs.

IV. CONCLUSION

In summary, we have explored the impact of the topological charge on laser-driven electron dynamics in Weyl semimetals. For this purpose, multi-Weyl semimetals with topological charges $n = 1$, 2, and 3 are considered. It has been found that the laser-driven electronic currents are distinct for different n's. Moreover, the direction and amplitude of the current strongly depend on the laser polarization. The parity and amplitude of the Berry curvature determine the behavior of the anomalous current—current perpendicular to the laser polarization. As the laser's intensity increases, the scaling of the anomalous current with n deviates drastically from the linear response theory, i.e., $\mathbf{J_{\Omega}} \propto n$. Owing to the large linear response from the Berry curvature, the anomalous current dominates at lower intensity. However, the ratio of the anomalous current from higher to lower topological charge decreases, which leads the saturation of the anomalous current relatively at lower intensity. On the other hand, normal current—current parallel to the laser polarization—scales with the topological charge and therefore remains separated in magnitude at relatively higher intensity. As the intensity increases, the optical responses from multi-Weyl semimetals transit from a linear regime to a nonlinear regime, and from a perturbative regime to a nonperturbative regime. High-harmonic spectroscopy is used to probe the distinct and interesting features of the currents in multi-Weyl semimetals. It has been observed that the harmonic yield and the energy cutoff of the higher-order harmonics increase drastically as n increases. Moreover, the polarization of the emitted harmonics encodes information about the phase and magnitude of the Berry curvature's components. It can be anticipated that the topological charge of the multi-Weyl semimetal can be characterized by the polarization of the emitted harmonics in an all-optical way.

[1] N. P. Armitage, E. J. Mele, and A. Vishwanath, Rev. Mod. Phys. **90**, 015001 (2018).

[2] B. Yan and C. Felser, Annu. Rev. Condens. Matter Phys. **8**, 337 (2017).

[3] M. M. Vazifeh and M. Franz, Phys. Rev. Lett. **111**, 027201 (2013).

[4] Q. Li, D. E. Kharzeev, C. Zhang, Y. Huang, I. Pletikosić, A. Fedorov, R. Zhong, J. Schneeloch, G. Gu, and T. Valla, Nat. Phys. **12**, 550 (2016).

[5] S. Kaushik, D. E. Kharzeev, and E. J. Philip, Phys. Rev. B **99**, 075150 (2019).

[6] F. de Juan, A. G. Grushin, T. Morimoto, and J. E. Moore, Nat. Commun. **8**, 15995 (2017).

[7] Q. Ma, S.-Y. Xu, C.-K. Chan, C.-L. Zhang, G. Chang, Y. Lin, W. Xie, T. Palacios, H. Lin, S. Jia *et al.*, Nat. Phys. **13**, 842 (2017).

[8] D. Rees, K. Manna, B. Lu, T. Morimoto, H. Borrmann, C. Felser, J. Moore, D. H. Torchinsky, and J. Orenstein, Sci. Adv. **6**, eaba0509 (2020).

[9] C. Le and Y. Sun, J. Phys.: Condens. Matter **33**, 503003 (2021).

[10] C. Shekhar, N. Kumar, V. Grinenko, S. Singh, R. Sarkar, H. Luetkens, S.-C. Wu, Y. Zhang, A. C. Komarek, E. Kampert *et al.*, Proc. Natl. Acad. Sci. USA **115**, 9140 (2018).

[11] B. Meng, H. Wu, Y. Qiu, C. Wang, Y. Liu, Z. Xia, S. Yuan, H. Chang, and Z. Tian, APL Mater. **7**, 051110 (2019).

[12] S. A. Yang, H. Pan, and F. Zhang, Phys. Rev. Lett. **115**, 156603 (2015).

[13] A. A. Burkov, Phys. Rev. Lett. **113**, 247203 (2014).

[14] M. Trescher, B. Sbierski, P. W. Brouwer, and E. J. Bergholtz, Phys. Rev. B **91**, 115135 (2015).

[15] H.-J. Kim, K.-S. Kim, J.-F. Wang, M. Sasaki, N. Satoh, A. Ohnishi, M. Kitaura, M. Yang, and L. Li, Phys. Rev. Lett. **111**, 246603 (2013).

[16] B. Q. Lv, T. Qian, and H. Ding, Rev. Mod. Phys. **93**, 025002 (2021).

[17] Y.-Y. Lv, J. Xu, S. Han, C. Zhang, Y. Han, J. Zhou, S.-H. Yao, X.-P. Liu, M.-H. Lu, H. Weng *et al.*, Nat. Commun. **12**, 6437 (2021).

[18] C. Bao, P. Tang, D. Sun, and S. Zhou, Nat. Rev. Phys. **4**, 33 (2021).

[19] J. Orenstein, J. Moore, T. Morimoto, D. Torchinsky, J. Harter, and D. Hsieh, Annu. Rev. Condens. Matter Phys. **12**, 247 (2021).

[20] R. M. A. Dantas, Z. Wang, P. Surówka, and T. Oka, Phys. Rev. B **103**, L201105 (2021).

[21] Y. Tamashevich, Leone Di Mauro Villari, and M. Ornigotti, Phys. Rev. B **105**, 195102 (2022).

[22] F. Nathan, I. Martin, and G. Refael, Phys. Rev. Res. **4**, 043060 (2022).

[23] O. Matsyshyn, F. Piazza, R. Moessner, and I. Sodemann, Phys. Rev. Lett. **127**, 126604 (2021).

[24] S. Ahn, E. J. Mele, and H. Min, Phys. Rev. B **95**, 161112(R) (2017).

[25] N. Sirica and R. Prasankumar, Nat. Mater. **20**, 283 (2021).

[26] G. B. Osterhoudt, L. K. Diebel, M. J. Gray, X. Yang, J. Stanco, X. Huang, B. Shen, N. Ni, P. J. Moll, Y. Ran *et al.*, Nat. Mater. **18**, 471 (2019).

[27] Y. Gao, S. Kaushik, E. Philip, Z. Li, Y. Qin, Y. Liu, W. Zhang, Y. Su, X. Chen, H. Weng *et al.*, Nat. Commun. **11**, 720 (2020).

[28] B. Q. Lv, H. M. Weng, B. B. Fu, X. P. Wang, H. Miao, J. Ma, P. Richard, X. C. Huang, L. X. Zhao, G. F. Chen, Z. Fang, X. Dai, T. Qian, and H. Ding, Phys. Rev. X **5**, 031013 (2015).

[29] S.-Y. Xu, N. Alidoust, I. Belopolski, Z. Yuan, G. Bian, T.-R. Chang, H. Zheng, V. N. Strocov, D. S. Sanchez, G. Chang *et al.*, Nat. Phys. **11**, 748 (2015).

[30] N. Morali, R. Batabyal, P. K. Nag, E. Liu, Q. Xu, Y. Sun, B. Yan, C. Felser, N. Avraham, and H. Beidenkopf, Science **365**, 1286 (2019).

[31] D. Liu, A. Liang, E. Liu, Q. Xu, Y. Li, C. Chen, D. Pei, W. Shi, S. Mo, P. Dudin *et al.*, Science **365**, 1282 (2019).

[32] I. Belopolski, K. Manna, D. S. Sanchez, G. Chang, B. Ernst, J. Yin, S. S. Zhang, T. Cochran, N. Shumiya, H. Zheng *et al.*, Science **365**, 1278 (2019).

[33] C. Fang, M. J. Gilbert, X. Dai, and B. A. Bernevig, Phys. Rev. Lett. **108**, 266802 (2012).

[34] S.-M. Huang, S.-Y. Xu, I. Belopolski, C.-C. Lee, G. Chang, T.-R. Chang, B. Wang, N. Alidoust, G. Bian, M. Neupane *et al.*, Proc. Natl. Acad. Sci. U.S.A. **113**, 1180 (2016).

[35] G. Xu, H. Weng, Z. Wang, X. Dai, and Z. Fang, Phys. Rev. Lett. **107**, 186806 (2011).

[36] Q. Liu and A. Zunger, Phys. Rev. X **7**, 021019 (2017).

[37] S. Roy and A. Narayan, J. Phys.: Condens. Matter **34**, 385301 (2022).

[38] B.-J. Yang and N. Nagaosa, Nat. Commun. **5**, 4898 (2014).

[39] T. Nag, A. Menon, and B. Basu, Phys. Rev. B **102**, 014307 (2020).

[40] Z.-M. Huang, J. Zhou, and S.-Q. Shen, Phys. Rev. B **96**, 085201 (2017).

[41] S. Nandy, C. Zeng, and S. Tewari, Phys. Rev. B **104**, 205124 (2021).

[42] A. Menon and B. Basu, J. Phys.: Condens. Matter **33**, 045602 (2021).

[43] A. Menon, S. Chattopadhay, and B. Basu, Phys. Rev. B **104**, 075129 (2021).

[44] T. Nag and D. M. Kennes, Phys. Rev. B **105**, 214307 (2022).

[45] Q. Chen and G. A. Fiete, Phys. Rev. B **93**, 155125 (2016).

[46] E. V. Gorbar, V. A. Miransky, I. A. Shovkovy, and P. O. Sukhachov, Phys. Rev. B **96**, 155138 (2017).

[47] S. Park, S. Woo, E. J. Mele, and H. Min, Phys. Rev. B **95**, 161113(R) (2017).

[48] S. Nandy, S. Manna, D. Călugăru, and B. Roy, Phys. Rev. B **100**, 235201 (2019).

[49] R. M. A. Dantas, F. Peña-Benitez, B. Roy, and P. Surówka, Phys. Rev. Res. **2**, 013007 (2020).

[50] M. Mrudul, Á. Jiménez-Galán, M. Ivanov, and G. Dixit, Optica **8**, 422 (2021).

[51] M. S. Mrudul and G. Dixit, Phys. Rev. B **103**, 094308 (2021).

[52] L. Yue and M. B. Gaarde, J. Opt. Soc. Am. B **39**, 535 (2022).

[53] F. Nematollahi, S. A. Oliaei Motlagh, J.-S. Wu, R. Ghimire, V. Apalkov, and M. I. Stockman, Phys. Rev. B **102**, 125413 (2020).

[54] L. H. Thong, C. Ngo, H. T. Duc, X. Song, T. Meier *et al.*, Phys. Rev. B **103**, 085201 (2021).

[55] J. Gu and M. Kolesik, Phys. Rev. A **106**, 063516 (2022).

[56] A. Bharti, M. S. Mrudul, and G. Dixit, Phys. Rev. B **105**, 155140 (2022).

[57] See Supplemental Material at http://link.aps.org/supplemental/10.1103/PhysRevB.107.224308 for Berry curvature's components for multi-Weyl semimetals with different topological charges, comparison of the anomalous current with the current originating solely from the Berry curvature, and variation in the anomalous current with respect to the distance between the Weyl nodes at a laser intensity of 10^8 W/cm^2.

[58] D. Xiao, M.-C. Chang, and Q. Niu, Rev. Mod. Phys. **82**, 1959 (2010).

[59] H. K. Avetissian, V. N. Avetisyan, B. R. Avchyan, and G. F. Mkrtchian, Phys. Rev. A **106**, 033107 (2022).

[60] M. S. Mrudul, N. Tancogne-Dejean, A. Rubio, and G. Dixit, npj Comput. Mater. **6**, 10 (2020).

[61] O. Schubert, M. Hohenleutner, F. Langer, B. Urbanek, C. Lange, U. Huttner, D. Golde, T. Meier, M. Kira, S. W. Koch, and R. Huber, Nat. Photonics **8**, 119 (2014).

[62] M. Mrudul and G. Dixit, J. Phys. B: At., Mol. Opt. Phys. **54**, 224001 (2021).

[63] M. Hohenleutner, F. Langer, O. Schubert, M. Knorr, U. Huttner, S. W. Koch, M. Kira, and R. Huber, Nature (London) **523**, 572 (2015).

[64] B. Zaks, R. B. Liu, and M. S. Sherwin, Nature (London) **483**, 580 (2012).

[65] A. Pattanayak, M. S. Mrudul, and G. Dixit, Phys. Rev. A **101**, 013404 (2020).

[66] M. S. Mrudul, A. Pattanayak, M. Ivanov, and G. Dixit, Phys. Rev. A **100**, 043420 (2019).

[67] A. Pattanayak, S. Pujari, and G. Dixit, Sci. Rep. **12**, 6722 (2022).

[68] N. Rana and G. Dixit, Phys. Rev. A **106**, 053116 (2022).

[69] N. Rana, M. S. Mrudul, D. Kartashov, M. Ivanov, and G. Dixit, Phys. Rev. B **106**, 064303 (2022).

[70] D. Baykusheva, A. Chacón, J. Lu, T. P. Bailey, J. A. Sobota, H. Soifer, P. S. Kirchmann, C. Rotundu, C. Uher, T. F. Heinz *et al.*, Nano Lett. **21**, 8970 (2021).

[71] S. Kovalev, R. M. Dantas, S. Germanskiy, J.-C. Deinert, B. Green, I. Ilyakov, N. Awari, M. Chen, M. Bawatna, J. Ling *et al.*, Nat. Commun. **11**, 2451 (2020).

[72] B. Cheng, N. Kanda, T. N. Ikeda, T. Matsuda, P. Xia, T. Schumann, S. Stemmer, J. Itatani, N. P. Armitage, and R. Matsunaga, Phys. Rev. Lett. **124**, 117402 (2020).

[73] Y. Bai, F. Fei, S. Wang, N. Li, X. Li, F. Song, R. Li, Z. Xu, and P. Liu, Nat. Phys. **17**, 311 (2021).